

# Machine Detection of Enhanced Electromechanical Energy Conversion in $\text{PbZr}_{0.2}\text{Ti}_{0.8}\text{O}_3$ Thin Films

Joshua C. Agar,\* Ye Cao, Brett Naul, Shishir Pandya, Stéfan van der Walt, Aileen I. Luo, Joshua T. Maher, Nina Balke, Stephen Jesse, Sergei V. Kalinin, Rama K. Vasudevan, and Lane W. Martin\*

Many energy conversion, sensing, and microelectronic applications based on ferroic materials are determined by the domain structure evolution under applied stimuli. New hyperspectral, multidimensional spectroscopic techniques now probe dynamic responses at relevant length and time scales to provide an understanding of how these nanoscale domain structures impact macroscopic properties. Such approaches, however, remain limited in use because of the difficulties that exist in extracting and visualizing scientific insights from these complex datasets. Using multidimensional band-excitation scanning probe spectroscopy and adapting tools from both computer vision and machine learning, an automated workflow is developed to featurize, detect, and classify signatures of ferroelectric/ferroelastic switching processes in complex ferroelectric domain structures. This approach enables the identification and nanoscale visualization of varied modes of response and a pathway to statistically meaningful quantification of the differences between those modes. Among other things, the importance of domain geometry is spatially visualized for enhancing nanoscale electromechanical energy conversion.

Utilizing ferroic materials for energy harvesting, sensing, and multistate memory and logic hinges on the ability to drive structural/state reconfiguration under externally applied stimuli. Although at the unit-cell level ferroelectrics are intrinsically bistable, they can self-assemble into domain structures with a multitude of states. Manipulating such domain structure

using external stimuli can give rise to large extrinsic effects with the potential for multifold increases in ferroelectric susceptibilities.<sup>[1–3]</sup> Consequentially, studies of how ferroelectric domain structures respond under applied fields and impact functional response is a matter of great interest. Until recently, however, adequate metrologies capable of probing the stimuli-driven response of such structures at the appropriate length and time scales were not available. Instead, the response of these materials has been inferred from static or stroboscopic studies<sup>[4]</sup> combined with computational simulations.<sup>[5,6]</sup> The advent of in situ probes (e.g., piezoresponse force microscopy (PFM),<sup>[7,8]</sup> transmission electron microscopy (TEM),<sup>[9,10]</sup> and synchrotron-based diffraction<sup>[11]</sup>), however, now allows researchers to access, and image, material response under external stimuli at length and time scales

commensurate with the structure and its response. These approaches have led to orders-of-magnitude increase in the volume, variety, veracity, and velocity of the experimentally generated data, rendering conventional analysis approaches untenable.<sup>[12,13]</sup> The data from these experiments typically takes the form of a hyperspectral image (composed of a spectrum at

Dr. J. C. Agar, Dr. S. Pandya, A. I. Luo, J. T. Maher, Prof. L. W. Martin  
Department of Materials Science & Engineering  
University of California  
Berkeley, CA 94720, USA  
E-mail: jagar@berkeley.edu; lwmartin@berkeley.edu

Prof. Y. Cao  
Department of Materials Science and Engineering  
University of Texas Arlington  
Arlington, TX 76019, USA


Prof. Y. Cao, Dr. N. Balke, Dr. S. Jesse, Dr. S. V. Kalinin,  
Dr. R. K. Vasudevan  
Center for Nanophase Materials Sciences  
Oak Ridge National Laboratory  
Oak Ridge, TN 37831, USA

Prof. Y. Cao, Dr. N. Balke, Dr. S. Jesse, Dr. S. V. Kalinin,  
Dr. R. K. Vasudevan  
Institute for Functional Imaging of Materials  
Oak Ridge National Laboratory  
Oak Ridge, TN 37831, USA

Dr. B. Naul  
Department of Astronomy  
University of California  
Berkeley, Berkeley, CA 94720, USA

Dr. S. van der Walt  
Berkeley Institute of Data Science  
University of California  
Berkeley, Berkeley, CA 94720, USA

Prof. L. W. Martin  
Materials Sciences Division  
Lawrence Berkeley National Laboratory  
Berkeley, CA 94720, USA

 The ORCID identification number(s) for the author(s) of this article can be found under <https://doi.org/10.1002/adma.201800701>.

DOI: 10.1002/adma.201800701

each pixel) which,<sup>[14]</sup> when coupled with the volume of data, makes it incomprehensible to visualize without dimensionality reduction (i.e., creating lower dimensional projections).

Traditionally, analysis of such hyperspectral data has relied on brute-force approaches wherein human-designed empirical functions are used to extract parameters of predetermined significance.<sup>[15,16]</sup> This approach is only possible when the spectra are well-behaved, and of a simple and consistent form (i.e., physically defined by linear, exponential, etc. functions). This approach fails to identify or can even misrepresent results when the data has unknown variety (i.e., different mathematical forms or different mechanisms of response), veracity (or uncertainty), and/or requires analysis of high-velocity data (e.g., data streams for instantaneous detection and control). Furthermore, these approaches are unsuitable when the physical mechanisms of the response are unknown and/or the response has fine-features.<sup>[17,18]</sup> Alternatively, machine learning can be employed to identify statistical correlations, trends, clusters, and anomalies which simplify the visualization and extraction of scientific insight.<sup>[7,19–21]</sup> While the fields of astronomy,<sup>[22]</sup> climate modeling,<sup>[23]</sup> protein crystallography,<sup>[24]</sup> and genomics<sup>[25]</sup> have included machine learning in their daily lexicon, it has yet to be sufficiently embraced in experimental materials science.<sup>[14,20,26]</sup> Although single-step machine-learning approaches, including dimensionality reduction using principal and independent component analysis,<sup>[27,28]</sup> end-member extraction using N-FINDR<sup>[27]</sup> and Bayesian linear unmixing,<sup>[29]</sup> clustering using *k*-means clustering,<sup>[30]</sup> and classification,<sup>[31]</sup> have been applied to nanoscale spectroscopy,<sup>[32,33]</sup> early endeavors in this regard have not created machine-learning workflows specifically designed to extract statistical insight about physical phenomena in materials, in turn, this has limited both the sensitivity and specificity of the extracted insights.

Here, using band-excitation (BE) PFM and tools adapted from both computer vision and machine learning, we expand conventional machine learning approaches by designing a machine-learning workflow which includes a physically guided featurization step for the study of switching processes, that enables detection and classification of ferroelectric/ferroelastic switching events in complex ferroelectric domain structures. We evaluate our machine-learning model by testing it on  $\text{PbZr}_{0.2}\text{Ti}_{0.8}\text{O}_3$  thin films with *c/a/c/a* domain structures where the structure and switching mechanisms are well-established. We then apply this model to  $\text{PbZr}_{0.2}\text{Ti}_{0.8}\text{O}_3$  thin films with complex nanoscale hierarchical domain structures where the switching mechanisms are uncertain. Using this approach, we identify, visualize at the nanoscale, and provide statistically meaningful quantification of different modes of stimuli-driven responses including highlighting the role of domain geometry in ferroelastic switching. In particular, we show that certain boundaries between *c/a/c/a* and  $a_1/a_2/a_1/a_2$  domain bands have increased ferroelastic behavior under bias and, in turn, define an optimal domain geometry capable of maximizing electromechanical energy conversion. This work demonstrates how to build a machine-learning model to discover new scientific insight in experimental materials science. To facilitate the widespread implementation of these approaches, all data, codes, and analysis packages are provided as a python-based executable Jupyter notebook (Figures S1 and S2, Supporting Information).<sup>[34]</sup> Ultimately, this work represents an important example of how the confluence of multidimensional spectroscopy

and machine learning can aid our understanding and design of ferroelectric materials, and how such approaches can be broadly applied to the analysis of hyperspectral experimental data.

To demonstrate the methodology, we begin with analysis of 100 nm  $\text{PbZr}_{0.2}\text{Ti}_{0.8}\text{O}_3$ /30 nm  $\text{SrRuO}_3/\text{GdScO}_3$  (110) heterostructures grown using pulsed-laser deposition (the Experimental Section). Similar heterostructures have been extensively studied<sup>[2,16]</sup> and are known to exhibit *c/a/c/a* domain structures, with primarily out-of-plane polarized *c* domains and minority in-plane polarized *a* domains (Figure 1a; Figure S3, Supporting Information). To detect the switching process, we conducted PFM-based BE piezoresponse spectroscopy (BEPS; Experimental Section and Figures S4 and S5, Supporting Information). BEPS measures the voltage-dependent piezoelectric response during ferroelectric switching and extracts the amplitude (*A*), phase ( $\varphi$ ), resonance frequency ( $\omega$ ), and quality factor (*Q*) of the cantilever resonance which are qualitative measures of the piezoresponse, polarization direction, elastic modulus, and energy absorption, respectively (Figure S6, Supporting Information). The results from these experiments include 4D signal (*A*,  $\varphi$ ,  $\omega$ , *Q*), *L*-dimensional loop cycle (*L* = 1–4), 2D spatial (*x*, *y* = 50–60 points), and *V*-dimensional voltage (*V* = 64–128) data which, when combined, create a large dimensional data volume. Visualization of the switching process can be achieved by forming images (across *x*, *y*) of the signals (*A*,  $\varphi$ ,  $\omega$ , *Q*) at various voltage steps through the switching cycle (Figure 1a–c; Movie S1 and Figure S7, Supporting Information). Starting with the heterostructure in the up-poled state (green phase, inset Figure 1a), we observe enhanced out-of-plane piezoresponse in the *c* domains as compared to the *a* domains. Application of positive bias results in rapid ferroelectric (180°) switching at/near the *a* domains (Figure 1b). As the bias increases, the film eventually completes the switching process resulting in an identical down-poled structure (Figure 1c). When applying negative bias, the switching process proceeds in the same manner except with the opposite sense. This switching process is consistent with prior reports.<sup>[9,16]</sup>

An alternative approach to extract information from these experiments is to analyze the spatial dependence (*x*, *y*) of the piezoresponse loops ( $A \cos \varphi$ ) which have a similar form to macroscopic ferroelectric hysteresis loops (circles, Figure 1d). To visualize the spatial dependence of the loop shape, the convention is to fit the loops with an empirical 15-parameter function constrained to have the same shape as a ferroelectric hysteresis loop (red line, Figure 1d), allowing the creation of spatial maps of the fitting parameters (Figures S8–S14, Supporting Information).<sup>[16,35]</sup> In general, such fits appear to model the piezoresponse loops well; however, upon closer inspection it is found that the fits fail to capture the fine features of the switching process in the bottom branch, indicating that the function lacks the complexity to model the data precisely. Furthermore, it is not possible to increase the complexity of the fitting function as doing so could lead to overfitting, decreasing the physical inference contained within the fitted parameters. It should be noted that such fine features in the local hysteresis loops<sup>[17]</sup> and piezoelectric response behavior<sup>[18]</sup> have been observed previously, yet no means of accurately analyzing these features have been demonstrated.

We sought a route capable of better identifying and grouping all of the features associated with our understanding of the

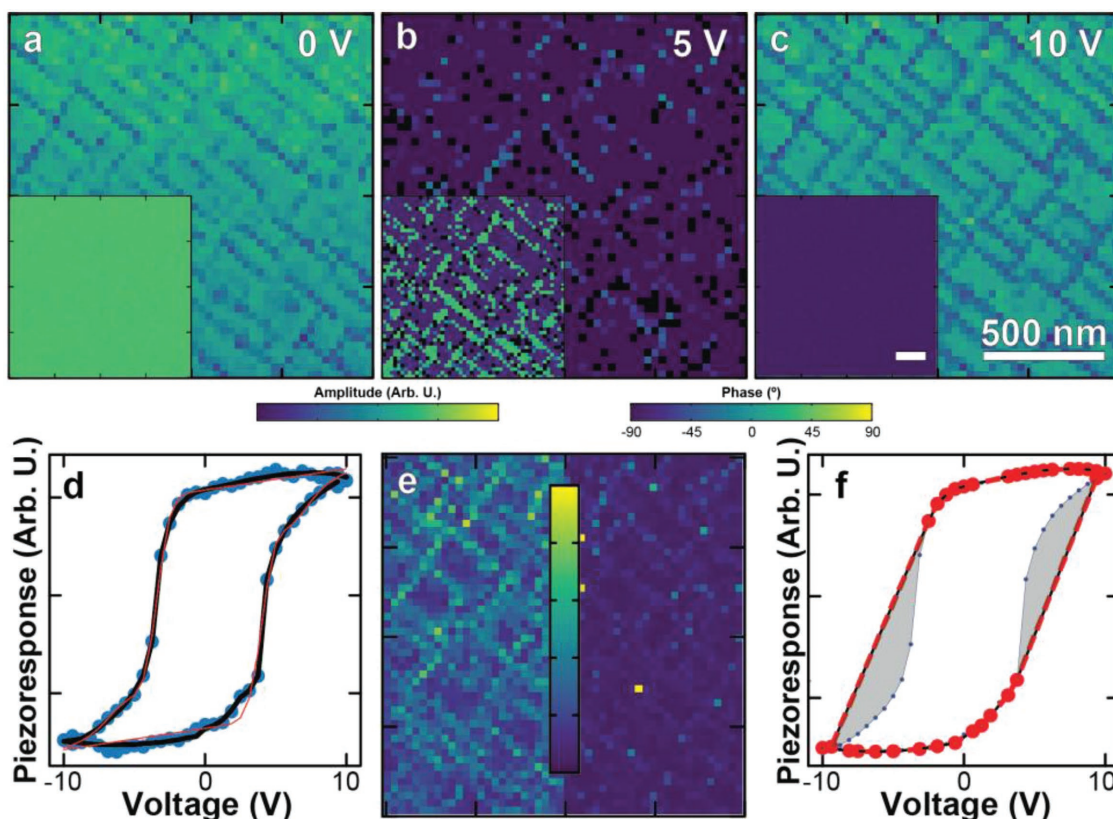


**Figure 1.** a–c) Band excitation piezoresponse force microscopy amplitude and phase images at various voltage steps throughout the switching cycle. d) Example piezoresponse hysteresis loop at a single pixel showing raw data (blue circles), loop fit results (red line), and low-rank approximation (black line). e) Maps of mean square error between the loop fit results (left), low-rank approximation (right), and the raw data. Results show that the low-rank approximation contains more of the original information than the loop fits results. f) Example convex hull construction of piezoresponse hysteresis loops (red). Markers indicate points on the convex polygon. Shaded region indicates the area used to create concavity curves.

switching process as probed by BEPS, including those not captured from the standard analyses. To enhance our sensitivity to switching mechanisms, beyond using the raw piezoresponse vector, or the principal components as a feature vector for clustering, we developed a machine-learning workflow which includes a featurization step. Inclusion of this featurization increases the sensitivity of the clustering algorithms to the switching phenomena. It is worth emphasizing that the design and selection of characteristic features is the most important and often the most difficult step in designing functional machine-learning workflows. For instance, in computer vision there are entire fields focused on developing feature extraction algorithms.<sup>[36]</sup> In piezoresponse hysteresis loops, the switching processes are marked by transitions between meta-/stable states. These transitions manifest as changes to the shape or geometry of the hysteresis loop, typically as convex features of the loop, and thus, the concave regions separating these points are indicative of switching events. In turn, we applied a geometric transformation to the piezoresponse loops to identify these transitions. Prior to applying these transformations, it was important to smooth the loops such that they are well-behaved, while preserving important structural features. To do this, principal-component-analysis (PCA)-based denoising was applied (Figures S15–17, Supporting Information).<sup>[37]</sup> Simply, this method builds a self-replication function (identity function)

which has enough capacity to preserve the important features in the data while eliminating the noise. We show an example of a denoised piezoresponse hysteresis loop (black line, Figure 1d); this low-rank approximation (using the first 15 principal components) matches all structural features of the piezoresponse hysteresis loop. Comparison of the mean-squared error of the 15-parameter functional fit (left, Figure 1e) and the denoised hysteresis loop (right, Figure 1e) to the raw data reveals that the denoised approximation is a better representation of the original data. This implies that the empirical function does not possess the capacity to fit all features of the piezoresponse.

To robustly quantify the concave features of the piezoresponse hysteresis loops, we adapted a convex-hull approach (i.e., the smallest convex polygon containing all the points<sup>[38]</sup>) used in computer vision to featurize shape complexity and concavities,<sup>[39]</sup> and applied it to the denoised piezoresponse hysteresis loops (Figure 1f; Figure S18, Supporting Information). In constructing the convex hull (red line, Figure 1f), the switching events are quantified by the region between the convex hull and the piezoresponse hysteresis loop. The resulting output is a sparse feature vector of the hysteresis loops that is sensitive to the switching processes. It is important to note that this featurization is not constrained to a model (as is the case with loop fitting) and thus allows the identification of new features/response modes not known a priori.



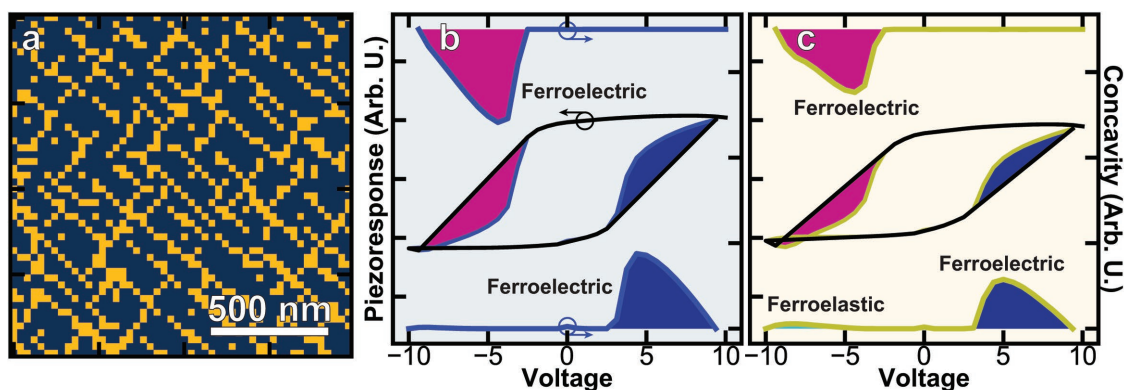


**Figure 2.** a) Cluster map obtained from *k*-means clustering of piezoelectric loop concavity of  $\text{PbZr}_{0.2}\text{Ti}_{0.8}\text{O}_3$  with *c/a/c/a* domain structures. b,c) Average piezoresponse hysteresis loop and loop concavity of clusters localized within the *c* domains (b) and *a* domains (c). Color of binary cluster map matches color of hysteresis loops and concavity curves.

Using the feature vector from the convex-hull construction, divisive hierarchical *k*-means clustering<sup>[40]</sup> can be used to cluster the switching processes. Briefly, this approach partitions the hysteresis loops into *k*-clusters wherein each of the observations (i.e., concavities) are assigned to one of *k*-clusters based on their distance from the centroids (the workflow for the entire machine-learning workflow is outlined in Figure S19, Supporting Information).<sup>[41]</sup> From the clustering map (Figure 2a), it is found that this methodology is able to detect differences in switching behavior corresponding to the domain structure. To evaluate our machine-learning workflow, we plot average piezoresponse hysteresis loops from within the clustered regions. Starting with the “blue” cluster identified within the *c* domains (Figure 2b), we observe classical square piezoresponse hysteresis loops with a single concavity/switching event indicative of a 180° ferroelectric switch. The average hysteresis loop from within the *a* domains or the “yellow” cluster (Figure 2c) reveals a similar form with the exception of additional concavities, most pronounced on the bottom branch. Additionally, there is evidence of a loop tail under negative saturation which has been attributed to ferroelastic domain-wall motion.<sup>[42]</sup> Combining these observations, we identify, as expected, a mixed ferroelectric–ferroelastic switching process which occurs at/near ferroelastic *a* domains. All told, these studies demonstrate the capabilities of this machine-learning workflow in identifying switching characteristics which match our well-established understanding of the domain structure and switching mechanism.

Having proven the capabilities of this approach on a material where the expected outcome/switching mechanism was already known, we applied this workflow to understand the switching processes in a more

complex and less understood system. To do this, 400 nm  $\text{PbZr}_{0.2}\text{Ti}_{0.8}\text{O}_3/30$  nm  $\text{Ba}_{0.5}\text{Sr}_{0.5}\text{RuO}_3/\text{NdScO}_3$  (110) heterostructures, were grown using pulsed-laser deposition (Experimental Section). These heterostructures reveal a hierarchical sawtooth-like surface topography (Figure 3a).<sup>[43]</sup> The sawtooth-like structure has periodicity on two length scales, a large-scale periodicity

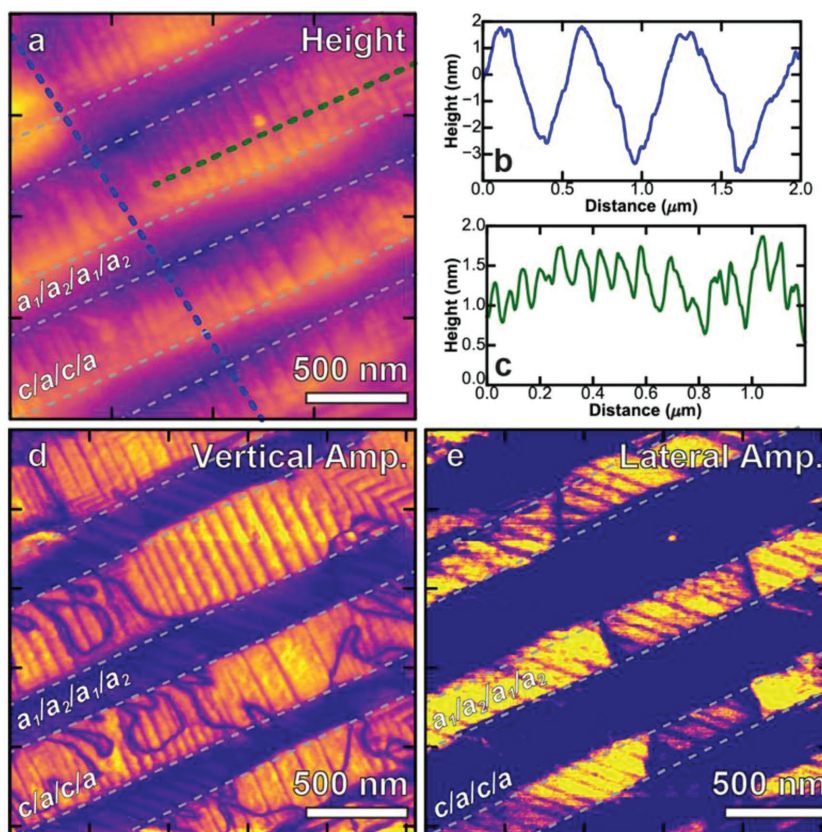


**Figure 3.** Piezoresponse force microscopy images of 400 nm  $\text{PbZr}_{0.2}\text{Ti}_{0.8}\text{O}_3$  heterostructures supported on  $\text{NdScO}_3$  (110). a) Topography, sections for line traces are indicated. b) Line trace indicating the large-scale sawtooth-like topography between the *c/a/c/a* and *a<sub>1</sub>/a<sub>2</sub>/a<sub>1</sub>/a<sub>2</sub>* domain bands. c) Line trace indicating the small-scale sawtooth-like topography within the *c/a/c/a* domain bands. d,e) Piezoresponse force microscopy images of the vertical (d) and lateral (e) amplitude.

with amplitude of  $\approx 4$  nm and a spacing of  $\approx 900$  nm peak-to-peak (Figure 3b), and a small-scale periodicity, within half of the bands, having an amplitude of  $\approx 0.5$  nm and a spacing of 30 nm peak-to-peak (Figure 3c). By comparing the vertical (Figure 3d) and lateral (Figure 3e) amplitude PFM images it is possible to develop a comprehensive picture of the domain structure. The bands with the small-scale sawtooth-like topography exhibit strong out-of-plane piezoresponse, whereas the smooth bands have suppressed out-of-plane piezoresponse. Within the bands with small-scale sawtooth-like topography there are fine linear domains with suppressed out-of-plane piezoresponse. Analysis of the lateral PFM images reveals enhanced in-plane piezoresponse

in the topographically smooth bands. Altogether, these studies reveal a hierarchical domain structure consisting of primarily out-of-plane polarized  $c/a/c/a$  bands and in-plane polarized  $a_1/a_2/a_1/a_2$  bands, which meet at the “peaks” and “valleys” of the large-scale sawtooth-like topography. This hierarchical domain structure emerges to accommodate the substrate induced tensile strain, which creates a nearly degenerate energy landscape between  $c/a/c/a$  and  $a_1/a_2/a_1/a_2$  domain variants (see the structural details in Figures S20 and S21, Supporting Information).

To understand the switching process in these heterostructures we started with visual inspection of initial and final PFM images in the switched region (Figure 4a,b). These images

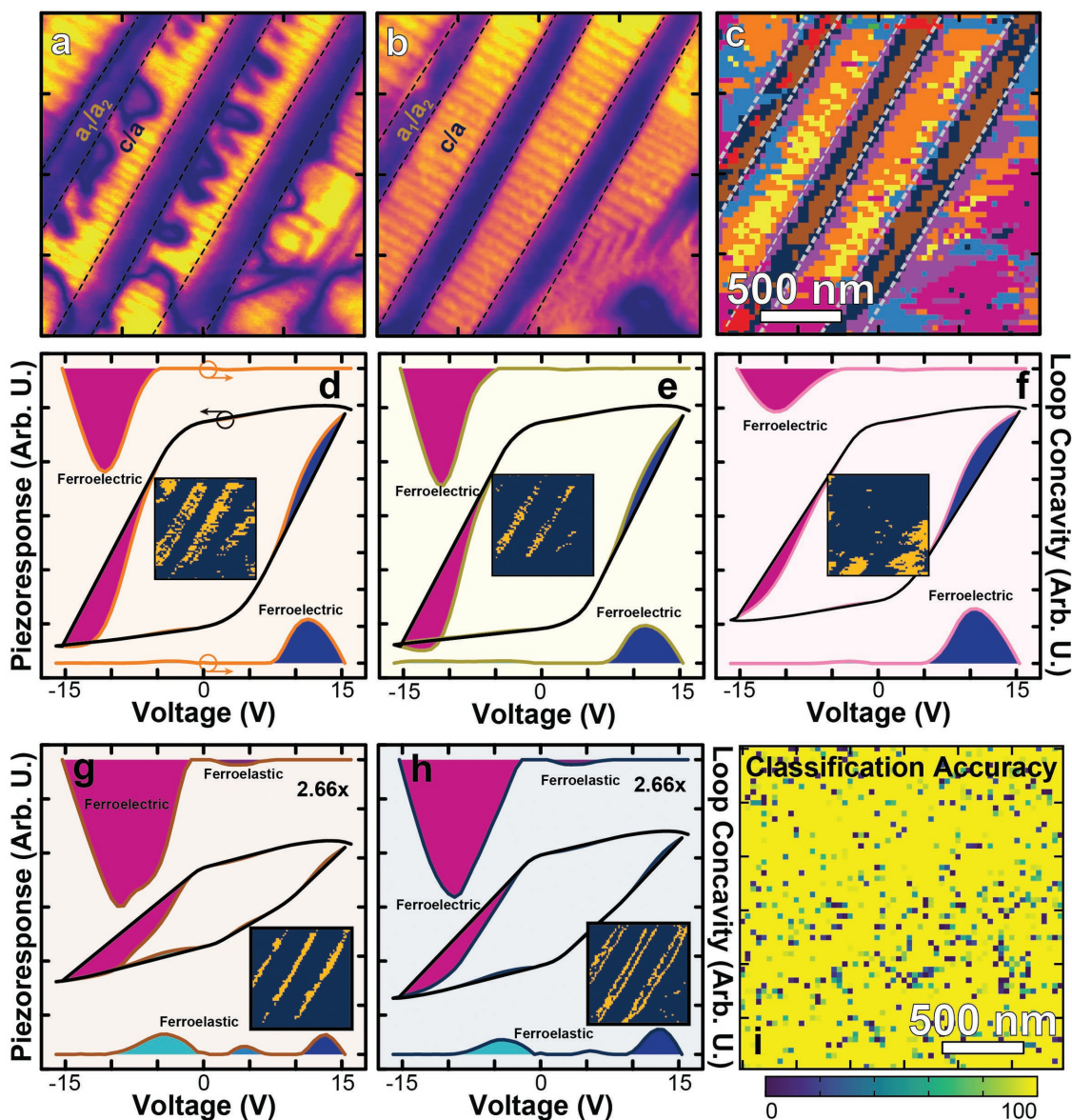


**Figure 4.** a,b) Piezoresponse force microscopy images taken prior to (a) and after (b) band excitation piezoresponse spectroscopy measurements. c)  $k$ -means clustering maps of piezoelectric loop concavity obtained from  $\text{PbZr}_{0.2}\text{Ti}_{0.8}\text{O}_3$  heterostructures with the hierarchical domain structures. d–f) Average piezoresponse hysteresis loop and loop concavity of three-out-of-four clusters identified within the  $c/a/c/a$  domain bands. g,h) Two-out-of-three clusters identified within the  $a_1/a_2/a_1/a_2$  domain bands. Transitions associated with ferroelectric and ferroelastic switching events are indicated. The inset shows binary cluster map indicating the region/cluster included in the average piezoresponse loops/concavity curves. Additional analysis of clustering results is provided in the Jupyter notebook. i) Map of classification accuracy as determined from 100  $k$ -nearest neighbor classifiers with random 80/20 test/train splits. Overall accuracy was  $\approx 92\%$ .



reveal changes in the domain structure that were not evident in our studies of heterostructures with  $c/a/c/a$  domain structures; namely the removal of  $180^\circ$  domain walls and ferroelastic domain reorientation (e.g., in the bottom right-hand corner of the image). Evidence of these structural transformations should exist in the BEPS; however, conventional BEPS analysis using the 15-parameter fitting function noted above suggests that the switching process is nearly indistinguishable from the heterostructures with  $c/a/c/a$  domain structures wherein only differences in the switching mechanisms between the  $c/a/c/a$  and  $a_1/a_2/a_1/a_2$  domain bands are obvious (Figures S22–S29 and Movie S2, Supporting Information). To uncover the unidentified features of the switching process, we applied our previously developed machine-learning workflow of using PCA to denoise the data (Figures S30–S32, Supporting Information), computation of the convex hull and extraction of piezoelectric concavity (Figure S33, Supporting Information), and subsequent  $k$ -means clustering to identify differences in the switching mechanism (details of the workflow in the Jupyter notebook; Figure S34, Supporting Information). From the clustering maps (Figure 4c), we identify a strong degree of spatial correlation with the domain structure; indicating that the clusters have physical significance. It is worth noting that both the PCA and the  $k$ -means clustering alone, while able to identify large differences in response, were insensitive to the fine-features of the switching process detected when using the convex-hull featurization (Figure S35, Supporting Information).

Starting our analysis of this cluster map within the  $c/a/c/a$  bands, clustering identifies three primary modes of response (Figure 4d–f). Spatially, two clusters occupy the  $c/a/c/a$  band in a striped pattern (Figure 4d,e) and the third is located primarily on the right-hand corner of the image. By comparing the average concavity curves, hysteresis loops, and initial and final domain structures, it is possible to understand the switching mechanisms identified by the machine-learning workflow. Starting with the “orange” cluster (Figure 4d), we observe a sharp single ferroelectric switching event, identical to the  $c$  domains in the heterostructures with  $c/a/c/a$  domain structures. Turning our attention to the “yellow” cluster (Figure 4e), we observe strong evidence of a tail (observed under negative saturation), identical to what was observed at the  $a$  domains in the heterostructures with  $c/a/c/a$  domain structures. Moving on to the “pink” cluster (Figure 4f), we observe highly tilted piezoresponse hysteresis loops (broad concavity curves) and suppressed piezoresponse. Returning to the initial/final PFM images, this cluster is localized to where the film underwent ferroelastic reordering, a process known to occur through successive ferroelastic switching events;<sup>[44]</sup> which explains the highly tilted, averaged piezoresponse hysteresis loops.

Changing our attention to the  $a_1/a_2/a_1/a_2$  bands, two clusters are identified; a “brown” cluster (Figure 4g) along the “valley” (right)  $c/a/c/a$ – $a_1/a_2/a_1/a_2$  boundary and a “blue” cluster which surrounds the “brown” cluster (Figure 4h). These clusters both show strong secondary concavities and highly tilted piezoresponse hysteresis loops indicative of a three-state, two-step  $c^+ \rightarrow a \rightarrow c^-$  ferroelastic switching process (additional experimental and phase-field evidence in Figures S36 and S37 and Movies S3–S5, Supporting Information). Upon closer inspection, it is evident that the ferroelastic character (i.e., the loop tilt

and magnitude of piezoelectric concavity) is more pronounced within the “brown” clusters (“valley” boundary) than the “blue” clusters (full clustering results are shown in Figure S38, Supporting Information).

To validate the robustness of our classification, we conducted cross-validation which simulates the veracity of the classifier by conducting a series of randomly sampled test/train splits wherein the classifier is trained on a subset of the data and its accuracy is evaluated on the test set (Figure S39, Supporting Information). Looking at the map of the classification accuracy (Figure 4i), we see that most of the map is classified with near-perfect accuracy ( $92 \pm 0.01\%$ ) and just a few pixels are responsible for a majority of the classification error.

Beyond the classification of the switching mechanism, we identified a variance in the ferroelastic character depending on the proximity to the “peak”/“valley”  $c/a/c/a$ – $a_1/a_2/a_1/a_2$  boundary that was not identified in any other manner. To quantitatively explore the ferroelastic character in the proximity of these boundaries, the piezoelectric concavities were fit with a summation of Gaussians (Figures S40 and S41, Supporting Information), allowing for quantification of the amplitude, voltage center, breadth, and area of each observed transition. Since the ferroelectric and ferroelastic transitions are highly localized in the voltage domain it is possible to bin the concavities based on the switching process they represent. Spatial maps of the concavity area for the ferroelectric (Figure 5a,b) and ferroelastic (Figure 5c,d) switching events of the bottom branch are provided (Figures S42–S47, Supporting Information). Spatial maps of the ferroelectric transition (Figure 5a) show increased ferroelectric character within the  $c/a/c/a$  bands. Within the  $a_1/a_2/a_1/a_2$  bands (Figure 5b), we observe a gradient in the ferroelectric character which is maximized (minimized) at the “peak” (“valley”)  $c/a/c/a$ – $a_1/a_2/a_1/a_2$  boundary. Conversely, the ferroelastic transition (Figure 5c) shows increased prominence within the  $a_1/a_2/a_1/a_2$  bands. Furthermore, we observe increased (suppressed) ferroelastic character along the “valley” (“peak”)  $c/a/c/a$ – $a_1/a_2/a_1/a_2$  boundary (Figure 5d).

Explanation of these observations requires consideration of the geometry and energetics of the domain structure during switching (Figure 5e). Again, the hierarchical domain structure consists of ordered  $c/a/c/a$  and  $a_1/a_2/a_1/a_2$  bands and these bands traverse the thickness of the film along the  $\{101\}$  to avoid forming a charged domain wall. Due to the asymmetry in out-of-plane lattice parameter between these two domain bands, the structure forms a sawtooth-like topography with “peaks” and “valleys,” determined by the tilt of the  $a_1/a_2/a_1/a_2$  band, which meets at the domain band boundaries. Switching (under positive bias) near the “peak” boundary (top, Figure 5f) occurs by nucleating a down-poled domain within the  $a_1/a_2/a_1/a_2$  band. This domain grows within the  $a_1/a_2/a_1/a_2$  band along the  $\{101\}$ . Upon reaching the  $c/a/c/a$  boundary, the domain can propagate by ferroelectric switching within the  $c/a/c/a$  band (bottom, Figure 5f). Throughout this process only a small volume is driven to switch ferroelastically, and thus its prominence in the piezoelectric loop is minimal. Since the nucleated ferroelastic domain must propagate along the  $\{101\}$ , when switching near the “valley” boundary this domain must propagate through the entire  $a_1/a_2/a_1/a_2$  band (top, Figure 5g). Only once this domain has traversed the  $a_1/a_2/a_1/a_2$  domain band can the region

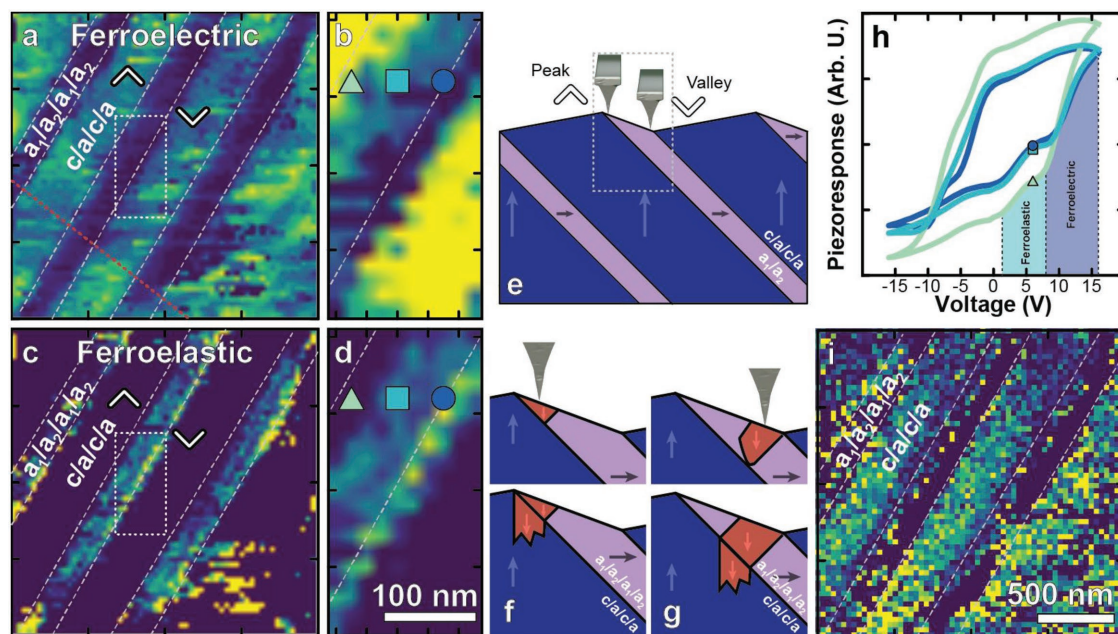


**Figure 5.** a–d) Maps of concavity area computed from Gaussian fits of ferroelectric (a,b) and ferroelastic (c,d) transitions. Dashed lines show the  $c/a/c/a$  and  $a_1/a_2/a_1/a_2$  domain bands. Triangle indicates the “peak” (up facing) and “valley” (down facing) boundaries. White-dashed box shows the region of interest within the  $a_1/a_2/a_1/a_2$  band. Note these graphs are rescaled to emphasize the features within the  $a_1/a_2/a_1/a_2$  band region. e) Schematic drawing of a cross-section of the hierarchical domain structure. f,g) Close-up near the surface showing switching process when the PFM tip is on the “peak” (left) (f) and “valley” (right) (g) side of the  $c/a/c/a$ - $a_1/a_2/a_1/a_2$  domain boundary. h) Example piezoresponse hysteresis loops traversing the  $a_1/a_2/a_1/a_2$  band. Loops correspond to colors/shapes indicated in (d). i) Map of cantilever resonance quality factor, an indication of the energy absorption properties of material. Image is taken at a voltage within the ferroelastic switching event as marked in (h).

switch ferroelectrically (bottom, Figure 5g), and in turn, this maximizes the volume that switches ferroelastically. To display this change in switching behavior we have provided example piezoresponse hysteresis loops traversing the  $a_1/a_2/a_1/a_2$  band (Figure 5h). These loops, as expected, have increased ferroelastic character on the “valley” (right) versus the “peak” (left)  $c/a/c/a$ - $a_1/a_2/a_1/a_2$  domain boundary. While rationalization of this observation might seem obvious in hindsight, one would have been unlikely to consider this effect in the absence of the machine-learning workflow which sifted through the data and brought this feature into focus. Furthermore, once this feature was established, this workflow allows for the quantification of effects with statistical significance and nanoscale resolution.

These ferroelastic transitions have practical implications for ferroelectric susceptibilities and, in particular, nanoscale electromechanical energy conversion. To visualize the enhanced electromechanical energy conversion potential, we plot a map of the cantilever quality factor at resonance during ferroelastic switching (Figure 5i). Increased dampening (manifested as a low quality factor) of the cantilever response at the “valley”  $c/a/c/a$ - $a_1/a_2/a_1/a_2$  boundary (where there is increased ferroelastic switching character) is observed wherein numerous pixels reveal complete quenching of the cantilever resonance, an indication that the material reversibly dampens or absorbs all energy from the sense pulse. This measurement of the energy absorption potential of the ferroelastic phase transformation is fundamentally different from large electromechanical actuation (like that reported in systems where ferroelastic transitions are possible)<sup>[45]</sup> and has implications for electromechanical energy

harvesting. At the same time, these observations also emphasize the importance of geometry, which in addition to domain volume fraction,<sup>[2,46]</sup> plays a significant role in electromechanical energy conversion. Specifically, when designing domain structures to maximize nanoscale electromechanical energy conversion it is desirable to maximize the volume fraction of the material that can undergo ferroelastic switching. Based solely on geometric considerations, an optimal geometry would have a domain width ( $w$ ) and film thickness ( $t$ ) where  $w > t\sqrt{2}$  such that the ferroelastic domain would propagate along the  $\{101\}$  through the thickness of the film prior to reaching the  $c/a/c/a$ - $a_1/a_2/a_1/a_2$  boundary where ferroelectric switching is permitted. Such a geometry could be accomplished by simply tuning the strain and film thickness in a thoughtful manner.

In summary, we develop a machine-learning workflow which includes a physically guided featurization step capable of instantaneously detecting and classifying nanoscale ferroelectric/ferroelastic switching processes. By developing this workflow on a well understood system with  $c/a/c/a$  domain structures we demonstrate the applicability of this approach. The workflow is then applied to glean new insights about switching processes in complex hierarchical domain structures. In turn, we identify the importance of, and define an optimal domain geometry for enhanced electromechanical energy conversion. This work shows the utility of using machine learning to identify variances in materials response relating to the structure concealed within multidimensional and hyperspectral data. This methodology has far-reaching implications in the understanding and controlled manipulation of polar order in ferroic systems, and also

could be applied more broadly to the analysis of fine features in hyperspectral data obtained from experimental techniques (e.g., current–voltage curves, electrochemical microscopy, nanorheology, etc.), and across scientific disciplines.

## Experimental Section

**Growth of Epitaxial  $\text{PbZr}_{0.8}\text{Ti}_{0.2}\text{O}_3$  Thin Films:** 100 nm (and 400 nm) thick  $\text{PbZr}_{0.8}\text{Ti}_{0.2}\text{O}_3$  thin films were synthesized via pulsed-laser deposition using a KrF excimer laser (248 nm, LPX 300, Coherent), in an on-axis geometry with a 60 mm target-to-substrate spacing. Films were grown on 30 nm  $\text{SrRuO}_3$ - (30 nm  $\text{Ba}_{0.5}\text{Sr}_{0.5}\text{RuO}_3$ -) buffered  $\text{GdScO}_3$  (110) [ $\text{NdScO}_3$  (110)] single-crystal substrates affixed to the heater using Ag-paint. The 100 nm thick  $\text{PbZr}_{0.8}\text{Ti}_{0.2}\text{O}_3$  layers were grown by ablating a  $\text{Pb}_{1.1}\text{Zr}_{0.8}\text{Ti}_{0.2}\text{O}_3$  ceramic target (Praxair) at a heater temperature of 600 °C in a dynamic oxygen pressure of 200 mtorr, at a laser fluence and repetition frequency of 1.9 J cm<sup>-2</sup> and 3 Hz, respectively. The  $\text{SrRuO}_3$  layers were grown at 630 °C in a dynamic oxygen pressure of 100 mtorr, at a laser fluence and repetition rate of 1.8 J cm<sup>-2</sup> and 13 Hz, respectively. For the 400 nm thick heterostructures, a  $\text{Ba}_{0.5}\text{Sr}_{0.5}\text{RuO}_3$  bottom electrode layer was grown at a heater temperature of 750 °C in a dynamic oxygen pressure of 20 mTorr, by ablating a  $\text{Ba}_{0.5}\text{Sr}_{0.5}\text{RuO}_3$  target (Praxair) at a laser fluence and repetition rate of 1.8 J cm<sup>-2</sup> and 2 Hz, respectively. Following growth, all heterostructures were cooled to room temperature in a static oxygen pressure of 760 Torr at 5 °C min<sup>-1</sup>.

**Band-Excitation Piezoresponse Spectroscopy (BEPS):** BEPS studies were performed at the Center for Nanophase Materials Science (CNMS) at Oak Ridge National Laboratory (ORNL) using a custom Cypher (Asylum Research) atomic force microscope controlled with a Labview- and Matlab-based controller. A bipolar-triangular-switching waveform was applied using a conductive scanning-probe tip in a square-grid measuring the cantilever response in the time domain. Following processing with a fast-Fourier transform, the cantilever resonance response was fit to a simple harmonic oscillator model, allowing the extraction of piezoresponse amplitude, phase, cantilever resonance frequency, and dissipation. The use of band excitation for these measurements is crucial as it minimizes effects from changing tip–sample contact resonances that can alter the observed response, enabling consistent measurements of piezoresponse throughout multiple dimensions (that is, frequency, spatial, voltage, time, and so on; Figures S4 and S5, Supporting Information). All measurements were carried out using Pt/Ir-coated probe tips (NanoSensor PPP-EFM). Switching spectroscopy measurements were measured at a resonance frequency of ≈1320 kHz (with a bandwidth of 60 kHz). The DC voltage was chosen such that the piezoelectric hysteresis loops were saturated in both the positive and negative direction. The local piezoresponse was measured at remanence (following a dwell time of 0.5 ms), with a BE waveform of sinc character (peak-to-peak voltage of 1 V).

**Machine-Learning-Based Classification of Piezoelectric Hysteresis Loops:** All computational analyses were completed in Python using open source software and packages. Machine learning-based principal component analysis, clustering, and fitting were completed using packages available in sci-kit learn.<sup>[47]</sup> Detailed descriptions of the analysis methodologies are provided in the Supporting Information. In addition, all raw data and analysis codes are provided as an executable and modifiable Jupyter notebook which can be explored within a web browser. The Jupyter notebook can be used to generate all plots included in the manuscript and Supporting Information as well as adjust the processing parameters for self-guided exploration of the data.

## Supporting Information

Supporting Information is available from the Wiley Online Library or from the author.

## Acknowledgements

Y.C. and B.N. contributed equally to this work. J.C.A. acknowledges partial support from the Army Research Office under grant W911NF-14-1-0104 and partial support of the U.S. Department of Energy, Office of Science, Office of Basic Energy Sciences, Materials Sciences and Engineering Division under Contract No. DE-AC02-05-CH11231; Materials Project program KC23MP. S.P. acknowledges support from the National Science Foundation under grant DMR-1708615. A.I.L. acknowledges support from the National Science Foundation under grant OISE-1545907. J.T.M. acknowledges support from the National Science Foundation under grant DMR-1451219. L.W.M. acknowledges support from the U.S. Department of Energy, Office of Science, Office of Basic Energy Sciences, under contract number DE-SC-0012375 for development of the ferroelectric thin films. The BEPS portion of this research was conducted at the Center for Nanophase Materials Sciences, which also provided support (S.V.K., R.K.V., S.J., N.B.) and is a US DOE Office of Science User Facility. The phase field simulations portion of this research was supported by the U.S. Department of Energy, Office of Science, Materials Sciences and Engineering Division (Y.C.). A portion of this research (B.N., S.v.d.W.) was sponsored by the Gordon and Betty Moore Foundation Data-Driven Discovery and (B.N.) NSF BIGDATA Grant no. 1251274.

## Conflict of Interest

The authors declare no conflict of interest.

## Keywords

domain structures, ferroelectric materials, machine learning, PZT, scanning-probe microscopy

Received: January 31, 2018

Revised: April 5, 2018

Published online: May 28, 2018

- [1] Q. M. Zhang, H. Wang, N. Kim, L. E. Cross, *J. Appl. Phys.* **1998**, *75*, 454.
- [2] J. Karthik, A. R. Damodaran, L. W. Martin, *Phys. Rev. Lett.* **2012**, *108*, 167601.
- [3] F. Xu, S. Trolier-McKinstry, W. Ren, B. Xu, Z. L. Xie, K. J. Hemker, *J. Appl. Phys.* **2000**, *89*, 1336.
- [4] A. R. Damodaran, C. W. Liang, Q. He, C. Y. Peng, L. Chang, Y. H. Chu, L. W. Martin, *Adv. Mater.* **2011**, *23*, 3170.
- [5] Y. H. Shin, I. Grinberg, I. W. Chen, A. M. Rappe, *Nature* **2007**, *449*, 881.
- [6] S. H. Baek, H. W. Jang, C. M. Folkman, Y. L. Li, B. Winchester, J. X. Zhang, Q. He, Y. H. Chu, C. T. Nelson, M. S. Rzchowski, X. Q. Pan, R. Ramesh, L. Q. Chen, C. B. Eom, *Nat. Mater.* **2010**, *9*, 309.
- [7] S. V. Kalinin, E. Strelcov, A. Belianinov, S. Somnath, R. K. Vasudevan, E. J. Lingerfelt, R. K. Archibald, C. Chen, R. Proksch, N. Laanait, S. Jesse, *ACS Nano* **2016**, *10*, 9068.
- [8] S. Somnath, L. Collins, M. A. Matheson, S. R. Sukumar, S. V. Kalinin, S. Jesse, *Nanotechnology* **2016**, *27*, 414003.
- [9] C. T. Nelson, P. Gao, J. R. Jokisaari, C. Heikes, C. Adamo, A. Melville, S.-H. Baek, C. M. Folkman, B. Winchester, Y. Gu, Y. Liu, K. Zhang, E. Wang, J. Li, L.-Q. Chen, C.-B. Eom, D. G. Schlom, X. Pan, *Science* **2011**, *334*, 968.
- [10] V. B. Ozdol, C. Gammer, X. G. Jin, P. Ercius, C. Ophus, J. Ciston, A. M. Minor, *Appl. Phys. Lett.* **2015**, *106*, 253107.
- [11] N. Laanait, W. Saenrang, H. Zhou, C.-B. Eom, Z. Zhang, *Adv. Struct. Chem. Imaging* **2017**, *3*, 11.



- [12] J. Hill, G. Mulholland, K. Persson, R. Seshadri, C. Wolverton, B. Meredig, *MRS Bull.* **2016**, *41*, 399.
- [13] S. Jesse, M. Chi, A. Belianinov, C. Beekman, S. V. Kalinin, A. Y. Borisevich, A. R. Lupini, *Sci. Rep.* **2016**, *6*, 26348.
- [14] S. V. Kalinin, B. G. Sumpter, R. K. Archibald, *Nat. Mater.* **2015**, *14*, 973.
- [15] R. K. Vasudevan, M. B. Okatan, C. Duan, Y. Ehara, H. Funakubo, A. Kumar, S. Jesse, L.-Q. Chen, S. V. Kalinin, V. Nagarajan, *Adv. Funct. Mater.* **2013**, *23*, 81.
- [16] J. C. Agar, A. R. Damodaran, M. B. Okatan, J. Kacher, C. Gammer, R. K. Vasudevan, S. Pandya, L. R. Dedon, R. V. K. Mangalam, G. A. Velarde, S. Jesse, N. Balke, A. M. Minor, S. V. Kalinin, L. W. Martin, *Nat. Mater.* **2016**, *15*, 549.
- [17] S. V. Kalinin, S. Jesse, B. J. Rodriguez, Y. H. Chu, R. Ramesh, E. A. Eliseev, A. N. Morozovska, *Phys. Rev. Lett.* **2008**, *100*, 155703.
- [18] R. K. Vasudevan, M. B. Okatan, I. Rajapaksa, Y. Kim, D. Marincel, S. Trolrier-McKinstry, S. Jesse, N. Valanoor, S. V. Kalinin, *Sci. Rep.* **2013**, *3*, 2677.
- [19] J. Carrasquilla, R. G. Melko, *Nat. Phys.* **2017**, *13*, 431.
- [20] N. Wagner, J. M. Rondinelli, *Front. Mater.* **2016**, *3*, <https://doi.org/10.3389/fmats.2016.00028>.
- [21] N. Bonnet, *Adv. Imaging Electron Phys.* **2000**, *114*, 1.
- [22] B. Naul, J. S. Bloom, F. Pérez, S. van der Walt, *Nat. Astron.* **2018**, *2*, 151.
- [23] M. Prabhat, Y. Liu, J. Correa, E. Racah, S. Y. Oh, A. Khosrowshahi, D. A. Lavers, M. F. Wehner, W. Collins, in *AGU Fall Meeting Abstracts* **2015**.
- [24] K. Lindorff-Larsen, S. Piana, R. O. Dror, D. E. Shaw, *Science* **2011**, *334*, 517.
- [25] M. W. Libbrecht, W. S. Noble, *Nat. Rev. Genet.* **2015**, *16*, 321.
- [26] P. Raccuglia, K. C. Elbert, P. D. F. Adler, C. Falk, M. B. Wenny, A. Mollo, M. Zeller, S. A. Friedler, J. Schrier, A. J. Norquist, *Nature* **2016**, *533*, 73.
- [27] R. K. Vasudevan, M. Ziatdinov, S. Jesse, S. V. Kalinin, *Nano Lett.* **2016**, *16*, 5574.
- [28] R. K. Vasudevan, S. Zhang, M. B. Okatan, S. Jesse, S. V. Kalinin, N. Bassiri-Gharb, *J. Appl. Phys.* **2015**, *118*, 072003.
- [29] S. Somnath, A. Belianinov, S. V. Kalinin, S. Jesse, *Nat. Commun.* **2016**, *7*, 13290.
- [30] A. Belianinov, R. Vasudevan, E. Strelcov, C. Steed, S. M. Yang, A. Tselev, S. Jesse, M. Biegalski, G. Shipman, C. Symons, A. Borisevich, R. Archibald, S. Kalinin, *Adv. Struct. Chem. Imaging* **2015**, *1*, 6.
- [31] M. P. Nikiforov, V. V. Reukov, G. L. Thompson, A. A. Vertegel, S. Guo, S. V. Kalinin, S. Jesse, *Nanotechnology* **2009**, *20*, 405708.
- [32] J. C. Agar, S. Pandya, R. Xu, A. K. Yadav, *MRS Bull.* **2016**, *6*, 151.
- [33] M. Ziatdinov, S. Fujii, M. Kiguchi, T. Enoki, S. Jesse, S. V. Kalinin, *Nanotechnology* **2016**, *27*, 495703.
- [34] J. C. Agar, Y. Cao, B. Naul, S. Pandya, S. van der Walt, A. I. Luo, J. T. Maher, N. Balke, S. Jesse, S. V. Kalinin, R. K. Vasudevan, L. W. Martin, **2017**, <https://doi.org/10.5281/zenodo.1242656>.
- [35] R. K. Vasudevan, S. Jesse, Y. Kim, A. Kumar, S. V. Kalinin, *MRS Commun.* **2012**, *2*, 61.
- [36] A. I. Awad, M. Hassaballah, *Image Feature Detectors and Descriptors*, Springer, Cham **2016**.
- [37] I. Jolliffe, *Principal Component Analysis*, John Wiley & Sons, Ltd, Chichester, UK **2002**.
- [38] A. M. Andrew, *Inf. Process. Lett.* **1979**, *9*, 216.
- [39] J.-X. Du, X.-F. Wang, G.-J. Zhang, *Appl. Math. Comput.* **2007**, *185*, 883.
- [40] A. K. Jain, M. N. Murty, P. J. Flynn, *ACM Comput. Surv.* **1999**, *31*, 264.
- [41] D. Sculley, *Web-Scale K-Means Clustering*, ACM, New York, USA **2010**.
- [42] E. Strelcov, Y. Kim, J. C. Yang, Y. H. Chu, P. Yu, X. Lu, S. Jesse, S. V. Kalinin, *Appl. Phys. Lett.* **2012**, *101*, 192902.
- [43] A. R. Damodaran, S. Pandya, J. C. Agar, Y. Cao, R. K. Vasudevan, R. Xu, S. Saremi, Q. Li, J. Kim, M. R. McCarter, L. R. Dedon, T. Angsten, N. Balke, S. Jesse, M. Asta, S. V. Kalinin, L. W. Martin, *Adv. Mater.* **2017**, *29*, 1702069.
- [44] R. Xu, S. Liu, I. Grinberg, J. Karthik, A. R. Damodaran, A. M. Rappe, L. W. Martin, *Nat. Mater.* **2014**, *14*, 79.
- [45] Z. Kutnjak, J. Petzelt, R. Blinc, *Nature* **2006**, *441*, 956.
- [46] J. Karthik, J. C. Agar, A. R. Damodaran, L. W. Martin, *Phys. Rev. Lett.* **2012**, *109*, 257602.
- [47] F. Pedregosa, G. Varoquaux, A. Gramfort, V. Michel, B. Thirion, O. Grisel, M. Blondel, P. Prettenhofer, R. Weiss, V. Dubourg, J. Vanderplas, A. Passos, D. Cournapeau, M. Brucher, M. Perrot, É. Duchesnay, *J. Mach. Learn. Res.* **2011**, *12*, 2825.